Design, Dimensional Synthesis and Evaluation of a Novel 2-DOF Spherical RCM Mechanism for Minimally Invasive Surgery

Jianmin Li
Key Lab for Mechanism Theory and Equipment Design of Ministry of Education,
Tianjin University, Tianjin 300072, China
e-mail: mjli@tju.edu.cn

Jiatong Wang
Key Lab for Mechanism Theory and Equipment Design of Ministry of Education,
Tianjin University, Tianjin 300072, China
e-mail: jtwang2021@126.com

Jianchang Zhao
Key Lab for Mechanism Theory and Equipment Design of Ministry of Education,
Tianjin University, Tianjin 300072, China
e-mail: zhaojianchang@tju.edu.cn

Guowu Wei*
School of Science, Engineering and Environment, University of Salford
The Crescent, Salford, M5 4WT, United Kingdom
e-mail: g.wei@salford.ac.uk
Member ASME

ABSTRACT

With the development of minimally invasive surgery (MIS) technology, higher requirements are put forward for the performance of remote center of motion (RCM) manipulator. This paper presents the conceptual design of a novel two degrees of freedom (2-DOF) spherical RCM mechanism, whose axes of all revote joints share the same RCM. Compared with the existing design, the proposed mechanism indicates a compact design and high structure stability, and the same scissor-like linkage makes it easy to realize modular design. It also has the advantages of singularity free and motion decoupling in its workspace, which simplifies the

* Corresponding author

implementation and control of the manipulator. In addition, compared with the traditional spherical scissor linkage mechanism, the proposed mechanism adds a rotation constraint on the output shaft to provide better operating performance. In this paper, the kinematics and singularities of different cases are deduced and compared, and the kinematic model of the best case is established. According to the workspace and constraints in MIS, the optimal structural parameters of the mechanism are determined by dimensional synthesis with the goal of optimal global operation performance. Furthermore, a prototype is assembled to verify the performance of the proposed mechanism. The experimental results show that the 2-DOF prototype can provide a reliable RCM point. The compact design makes the manipulator have potential application prospects in MIS.

1 INTRODUCTION

The basic operation concept of MIS is to insert surgical instruments such as a laparoscope into a patient's body through a small incision, so as to carry out surgical operation inside the patient's body [1]. Robot-assisted MIS is widely used in clinical surgery because of its great advantages over traditional open surgery [2]. Limited by the constraints of the incision point on the patient, the motion of the surgical instruments is limited to 1-DOF translation along the entry axis and 3-DOF rotations around the entry point called *the remote center of motion (RCM)*. In recent decades, RCM mechanisms have attracted extensive interests from researchers in the fields of mechanisms and robotics.

Compared with controlling redundant joints and adding passive joints, an RCM mechanism constructed by mechanical constraint method has the characteristics of high safety and simple control algorithms [3, 4]. According to the structural characteristics, this type of mechanism can be divided into parallelogram RCM mechanism, arc RCM mechanism, spherical RCM mechanism, and parallel RCM mechanism etc. Li et al. [5]

proposed a type synthesis method for constructing 2-DOF planar RCM mechanisms with a virtual double parallelogram structure. Huang et al. [6] proposed the design of 2-DOF planar RCM mechanisms based on closed-loop coupling-cable-driven strategy. Through the analysis and determination of the transmission ratio, it provided a large workspace but low collision risk for MIS robot. Kuo et al. [7] proposed a novel 4-DOF parallel RCM robot, and the 4 DOFs are fully decoupled. However, due to the large space occupied by the robot, it is almost impossible for multiple instruments to work together. Chen et al. [8] proposed a spatial dual-arm parallel manipulator with 3R1T (where R denotes rotation, and T stands for translation) motion capability, it provides better flexibility but has the disadvantage of occupying too much space. In order to reduce the space occupied by the robot and prevent the collision among the multi-robot system, Chen and his colleagues [9, 10] developed a new RCM mechanism based on double-triangular linkage.

In some operations, such as the abdominal surgery, three to four RCM operating arms are often required to work simultaneously. This means higher requirements for the compactness of the robots, especially in the retracted state. Hence, researchers are continuously looking for better mechanisms and solutions.

The axes of a spherical mechanism intersect at one point, and the links all move on the concentric spherical surfaces, and the intersection of the axes is the remote center of motion (RCM). Spherical mechanism has been applied to portable MIS robot [11], force reflection robot MC^2E [12] and the others. On the other hand, scissor-like mechanisms have good expansibility, high volume expansion rate and are easy to fabricate and assemble. Such mechanisms have wide applications in aerospace, novel buildings, and other fields [13]. The spherical scissor-like linkage mechanisms combine the advantages of the spherical and scissor-like mechanisms, and have found applications in the fields of shoulder rehabilitation [14] and architecture design [15]. Kocabas [16] designed a spherical gripper using a network of spherical parallelogram mechanisms, the gripper has only 1-DOF for grasping many shapes. Castro et al. [17] applied the spherical scissor-like linkages to the shoulder mechanism, and simplified the design of a spatial spherical mechanism. In this work, all the joints are passive and the positioning accuracy of the mechanism has not been verified. Afshar et al. [18] optimized the spherical scissor-like-linkage RCM robot for the task of ultrasonic scanning. In which, the singularity occurs when all the linkages collapse to the same plane in the limit position state, and the output shaft of the robot rotates along with the end link, which is not conducive to the control of the operating instruments.

According to the requirements of the MIS, a novel spherical RCM mechanism is proposed in this paper. The proposed mechanism indicates a compact design and high structure stability. In the retracted state, the compact structure effectively avoids the collision with the surrounding mechanical arms. It also has the advantages of singularity free and motion decoupling in its workspace. The same scissor-like linkage makes it easy to realize modular design, which has potential to adapt to different angles of workspace in different operations through changing the number of motion units. In addition, based on the traditional spherical scissor-like linkage RCM mechanism, the rotation constraint on the output shaft is added to provide a stable rotating base for the surgical instrument.

The rest of this paper is arranged as follows. In Sec. 2, the alternative cases of drive unit are selected through the kinematics and singularity analysis results. In Sec. 3, the characteristics of the proposed two output units are compared and analyzed. Then, in Sec. 4, based on the analysis of the first two sections, the series structure composed of several identical spherical four-bar units combined with planar constraint branch is selected as the final solution, and the dimensional synthesis is carried out with the goal of optimal global operation performance. In Sec. 5, a physical prototype is design and developed according to the optimal structural parameters, and the performance is tested through experiments. Conclusions are addressed in Sec. 6

2 Conceptual Design of the Drive Unit

In MIS operation, the surgical instrument holder needs to carry the surgical instrument to adjust the pitch and yaw attitude angle. As shown in Fig. 1(a), the traditional spherical RCM mechanisms normally use 2-DOF rotations through two arc links in series to achieve the desired function. Large-scale pitching workspace will lead to the excessive size of the links, and the width of the whole mechanism will be very large in the retracted state.

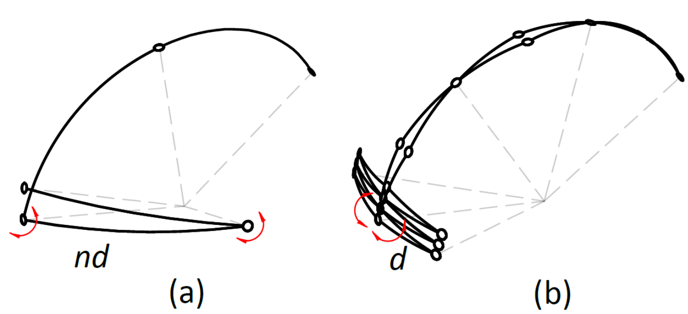

Fig. 1 Comparison of two kinds of spherical RCM mechanisms. (a) traditional spherical mechanism, and (b) the proposed spherical scissor-like linkage mechanism

As shown in Fig. 1(b), in order to ensure a small volume space ratio, n spherical scissor-like units are considered to be connected in series. Under the condition of the same workspace, compared with the traditional spherical mechanism, the size of the links in the scissors-like linkage mechanism will be reduced by n times, and the overall structure will be more compact in the retracted state. On the other hand, the hybrid structure allows the integration of the motors in the fixed platform.

In order to drive a series of scissor-like link units, two drive links are required to connect them to the base. According to the location of the connection points, two solutions can be distinguished as shown in Fig. 2: (1) drive unit with zero-length ground link, and (2) drive unit with non-zero-length ground link.

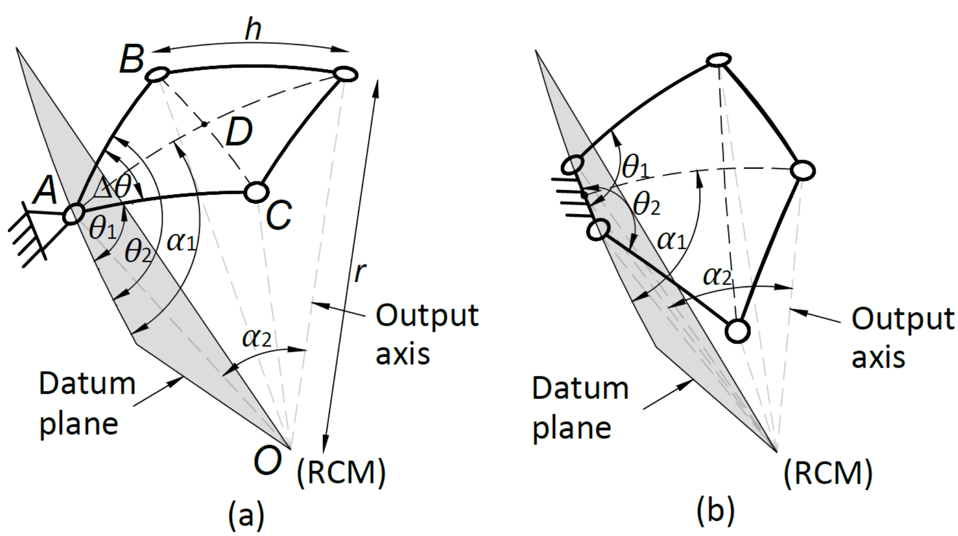

Fig. 2 Design of drive unit. (a) Case 1: drive unit with zero-length ground link, and (b) Case 2: drive unit with non-zero-length ground link

2.1 Analysis of Case 1

As shown in Fig. 2(a), drive unit with zero-length ground link consists of four curved links with the same angle h. All links keep moving on a spherical surface with radius r. The drive angles of the active links AC and AB are θ_1 and θ_2 respectively. The output axis is located on the symmetrical plane of the unit and its attitude angles are α_1 and α_2 respectively. To prevent singularity, let $h \in (0, \pi/2)$, $\alpha_2 \in (0, \pi)$.

2.1.1 Forward Kinematics

The pitch angle α_2 is uniquely determined by $\Delta\theta = (\theta_2 - \theta_1)$, let $\Delta\theta \in (0, \pi)$. According to the spherical cosine theorem and spherical Pythagorean theorem

$$\alpha_2 = 2\angle AOD = 2\cos^{-1}\left(\cos h / \cos(\angle BOC / 2)\right) \tag{1}$$

where $\cos\angle BOC = \cos^2 h + \sin^2 h \cos\Delta\theta$.

The yaw angle α_1 is determined by the angle bisector of the two drive angles. Thus, the forward kinematics equation of the mechanism is obtained as follows.

$$\begin{cases} \alpha_1 = 0.5(\theta_1 + \theta_2) \\ \alpha_2 = 2\cos^{-1}\left(\cos h / \cos(\angle BOC / 2)\right) \end{cases} \tag{2}$$

If transformations $\theta = (\theta_1 + \theta_2)$ and $\Delta\theta = (\theta_2 - \theta_1)$ are applied, it can be considered that the synthesized 2-DOF RCM motion is decoupled.

2.1.2 Inverse Kinematics

The inverse kinematics can be obtained by deducing the forward kinematics in reverse.

$$\begin{cases} \theta_1 = \alpha_1 - 0.5\cos^{-1}\left(\left(\cos\left(2\cos^{-1}\left(\cos h / \cos 0.5\alpha_2\right)\right) - \cos^2 h\right) / \sin^2 h\right) \\ \theta_2 = \alpha_1 + 0.5\cos^{-1}\left(\left(\cos\left(2\cos^{-1}\left(\cos h / \cos 0.5\alpha_2\right)\right) - \cos^2 h\right) / \sin^2 h\right) \end{cases} \tag{3}$$

2.1.3 Singularity

The relationship between joint velocity and end velocity can be described by the Jacobian matrix.

$$\boldsymbol{v} = \boldsymbol{J}\dot{\boldsymbol{\theta}} \tag{4}$$

$$\boldsymbol{J} = \begin{bmatrix} \frac{\partial \alpha_1}{\partial \theta_1} & \frac{\partial \alpha_1}{\partial \theta_2} \\ \frac{\partial \alpha_2}{\partial \theta_1} & \frac{\partial \alpha_2}{\partial \theta_2} \end{bmatrix} = \begin{bmatrix} 0.5 & 0.5 \\ -\frac{\sin^2 h \cdot \cos h \cdot \sin M \cdot \sin \Delta\theta}{\sqrt{1-\cos^2 2M} \cdot \sin 0.5\alpha_2 \cdot \cos^2 M} & \frac{\sin^2 h \cdot \cos h \cdot \sin M \cdot \sin \Delta\theta}{\sqrt{1-\cos^2 2M} \cdot \sin 0.5\alpha_2 \cdot \cos^2 M} \end{bmatrix} \tag{5}$$

where $M = 0.5\cos^{-1}\left(\cos^2 h + \sin^2 h \cdot \cos\Delta\theta\right)$.

Singularity occurs when the value of Jacobian determinant is 0, and the solution is $\Delta\theta = 0$ or π, and $h = \pi$ or 0.5π. As shown in Fig. 3, when $\Delta\theta = \pi$, the drive unit is fully retracted, all links overlap into one plane, and a forward kinematics singularity occurs. When $\Delta\theta = 0$, the drive unit is fully expanded, resulting in an uncontrollable degree of freedom. When $h = 0.5\pi$, the drive unit loses its ability to extend. Similarly, $h = \pi$ is also a singular state.

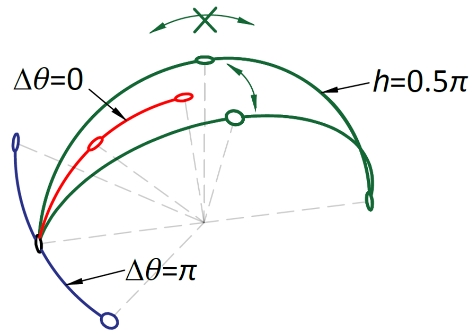

Fig. 3 Singularity of drive unit with zero-length ground link

2.2 Analysis of Case 2

As shown in Fig. 4, drive unit with non-zero-length ground link consists of five curved links. Link BD is the base of the motion unit, $\angle AOB = \angle AOD = h_1$. The drive angles of the active links BC and DE are θ_1 and θ_2 respectively, and they are both in the range of $(0, \pi)$. It is known that, $\angle BOC = \angle DOE = h_2$, $\angle COG = \angle GOE = h$, and the angles of all links are less than $\pi / 2$. The attitude angles of output axis α_1 and α_2 are shown in Fig. 2(b).

2.2.1 Forward Kinematics

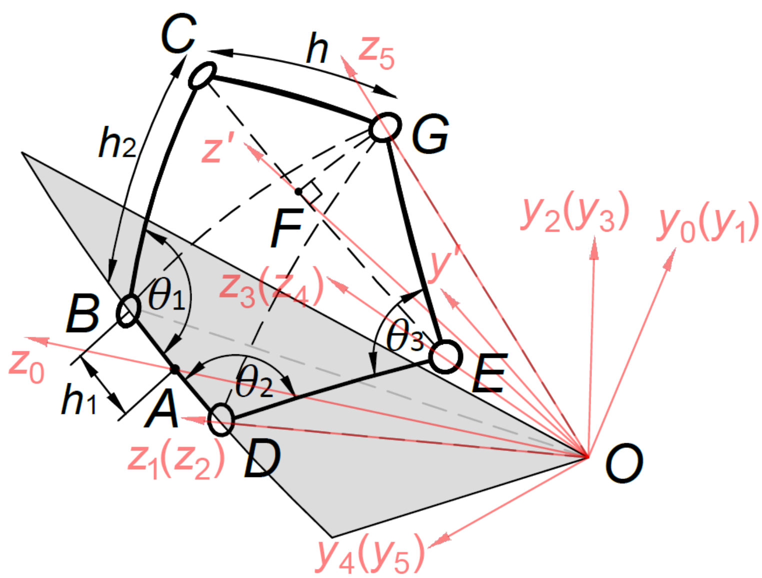

Fig. 4 Drive unit with non-zero-length ground link

As shown in Fig. 4, establish the reference coordinate systems at each joint and let the z -axes pass through the joint axes. The y -axes are perpendicular to the planes determined by the links and point to the center of the unit, and the x -axes are determined by the right-hand screw rule. The z_0 -axis of the base coordinate system passes through point A.

Then vector $\boldsymbol{OC}$ and vector $\boldsymbol{OE}$ can be expressed as

$$\boldsymbol{OC} = \boldsymbol{R}_y(-h_1)\cdot\boldsymbol{R}_z(\theta_1-\pi)\cdot\boldsymbol{R}_y(-h_2)\cdot\boldsymbol{z}, \quad \boldsymbol{OE} = \boldsymbol{R}_y(h_1)\cdot\boldsymbol{R}_z(\pi-\theta_2)\cdot\boldsymbol{R}_y(h_2)\cdot\boldsymbol{z} \tag{6}$$

Where $\boldsymbol{R}_y$ and $\boldsymbol{R}_z$ represent the rotation matrix around the y -axis and z -axis respectively, $\boldsymbol{R}_y(\chi)=\begin{bmatrix}\cos\chi & 0 & \sin\chi\\ 0 & 1 & 0\\ -\sin\chi & 0 & \cos\chi\end{bmatrix}$, $\boldsymbol{R}_z(\phi)=\begin{bmatrix}\cos\phi & -\sin\phi & 0\\ \sin\phi & \cos\phi & 0\\ 0 & 0 & 1\end{bmatrix}$.

Establish an intermediate coordinate system through the $\boldsymbol{OF}$ axis, and the direction of each coordinate axis is

$$\boldsymbol{z}' = \boldsymbol{OF} = \boldsymbol{OC} + \boldsymbol{OE}, \boldsymbol{y}' = \boldsymbol{EC} = \boldsymbol{OC} - \boldsymbol{OE}, \boldsymbol{x}' = \boldsymbol{y}' \times \boldsymbol{z}' \tag{7}$$

Thus, the rotation matrix of the intermediate coordinate system can be obtained

$$\boldsymbol{R_1} = \begin{bmatrix} \dfrac{\boldsymbol{x}'}{|\boldsymbol{x}'|} & \dfrac{\boldsymbol{y}'}{|\boldsymbol{y}'|} & \dfrac{\boldsymbol{z}'}{|\boldsymbol{z}'|} \end{bmatrix} \tag{8}$$

$\angle FOG$ can be expressed as

$$\angle FOG = \cos^{-1}\left(\cos h / \cos\left(\cos^{-1}\left(\boldsymbol{OC} \cdot \boldsymbol{OE}\right) / 2\right)\right) \tag{9}$$

Finally, the vector of the output axis can be obtained

$$\boldsymbol{OG} = \boldsymbol{R_1} \cdot \boldsymbol{R}_y\left(\angle FOG\right) \cdot \boldsymbol{z} \tag{10}$$

According to the above analysis, it can be seen that the forward kinematics of drive unit with non-zero-length ground link is extremely complex. Substituting Eqs. (6-9) into Eq. (10) will get a lengthy analytical equation, which severely limits the efficiency of kinematics calculation and is not appropriate for real-time control of the robot in practical applications.

2.2.2 Inverse Kinematics

The inverse kinematics needs to use the given output axis vector $\boldsymbol{OG}$ to solve the drive angles θ_1 and θ_2 of two active links.

$$\angle BOG = \cos^{-1}\left(\boldsymbol{OB} \cdot \boldsymbol{OG}\right),\ \angle DOG = \cos^{-1}\left(\boldsymbol{OD} \cdot \boldsymbol{OG}\right) \tag{11}$$

Apply cosine theorem on the spherical ΔBCG, ΔBDG and ΔDEG.

$$
\begin{aligned}
\angle CBG &= \cos^{-1}\left(\frac{\cos h - \cos h_2 \cos\angle BOG}{\sin h_2 \sin\angle BOG}\right)\\
\angle EDG &= \cos^{-1}\left(\frac{\cos h - \cos h_2 \cos\angle DOG}{\sin h_2 \sin\angle DOG}\right)\\
\angle GBD &= \cos^{-1}\left(\frac{\cos\angle DOG - \cos 2h_1 \cos\angle BOG}{\sin 2h_1 \sin\angle BOG}\right)\\
\angle GDB &= \cos^{-1}\left(\frac{\cos\angle BOG - \cos 2h_1 \cos\angle DOG}{\sin 2h_1 \sin\angle DOG}\right)
\end{aligned}
\tag{12}
$$

Hence, referring to Fig. 4, the two driving angles θ_1 and θ_2 can be obtained as,

$$
\begin{cases}
\theta_1 = \angle CBG + \angle GBD\\
\theta_2 = \angle EDG + \angle GDB
\end{cases}
\tag{13}
$$

2.2.3 Singularity

The forward kinematics of drive unit with non-zero-length ground link is complex, and it is difficult to obtain Jacobian matrix. Consider dividing the drive unit and discuss the singularities of each part separately. Firstly, the singularity caused by link CG and link GE is similar to zero-length ground link drive unit. As shown in Fig. 5 (a), CG and GE have two collinear states. When overlapping collinear, there is an uncontrollable degree of freedom. When straightening collinear, it is a forward kinematics singularity.

The singularity caused by link DE and link EG can be solved by D-H parameter method. Suppose $\angle DEG$ is θ_3, the forward kinematics equation can be expressed as

$$
{}^0_5\boldsymbol{R} = {}^0_1\boldsymbol{R}\cdot{}^1_2\boldsymbol{R}\cdot{}^2_3\boldsymbol{R}\cdot{}^3_4\boldsymbol{R}\cdot{}^4_5\boldsymbol{R}
\tag{14}
$$

where ${}^{A}_{B}\boldsymbol{R}$ represents the rotation matrix of B coordinate system relative to A coordinate system, ${}^{0}_{1}\boldsymbol{R}=\boldsymbol{R}_y\left(h_1\right)$, ${}^{1}_{2}\boldsymbol{R}=\boldsymbol{R}_z\left(\pi-\theta_2\right)$, ${}^{2}_{3}\boldsymbol{R}=\boldsymbol{R}_y\left(h_2\right)$, ${}^{3}_{4}\boldsymbol{R}=\boldsymbol{R}_z\left(\pi-\theta_3\right)$, ${}^{4}_{5}\boldsymbol{R}=\boldsymbol{R}_y\left(h\right)$.

Thus,

$$
{}^{2}_{5}\boldsymbol{R}={}^{2}_{3}\boldsymbol{R}\cdot{}^{3}_{4}\boldsymbol{R}\cdot{}^{4}_{5}\boldsymbol{R}=\begin{bmatrix}-\mathrm{c}h_2\,\mathrm{c}\theta_3\,\mathrm{c}h-\mathrm{s}h_2\,\mathrm{s}h & \mathrm{c}h_2\,\mathrm{s}\theta_3 & \mathrm{c}h_2\,\mathrm{c}\theta_3\,\mathrm{s}h-\mathrm{s}h_2\,\mathrm{c}h\\ -\mathrm{s}\theta_3\,\mathrm{c}h & -\mathrm{c}\theta_3 & \mathrm{s}\theta_3\,\mathrm{s}h\\ -\mathrm{s}h_2\,\mathrm{c}\theta_3\,\mathrm{c}h+\mathrm{c}h_2\,\mathrm{s}h & \mathrm{s}h_2\,\mathrm{s}\theta_3 & \mathrm{s}h_2\,\mathrm{c}\theta_3\,\mathrm{s}h+\mathrm{c}h_2\,\mathrm{c}h\end{bmatrix},{}^{4}_{5}\boldsymbol{R}=\begin{bmatrix}\mathrm{c}h & 0 & -\mathrm{s}h\\ 0 & 1 & 0\\ \mathrm{s}h & 0 & \mathrm{c}h\end{bmatrix}\tag{15}
$$

According to the principle of differential transformation

$$
{}^{T}\boldsymbol{\omega}=\begin{bmatrix}{}^{T}\boldsymbol{J}_2 & {}^{T}\boldsymbol{J}_4\end{bmatrix}\begin{bmatrix}\dot{\theta}_2\\ \dot{\theta}_3\end{bmatrix}\tag{16}
$$

where ${}^{T}\boldsymbol{\omega}=\begin{bmatrix}{}^{T}\omega_x & {}^{T}\omega_y & {}^{T}\omega_z\end{bmatrix}^T$, indicating the angular velocity of the output axis relative to the end coordinate system. ${}^{T}\boldsymbol{J}_i$ represents the angular velocity caused by the unit joint velocity of joint i,

$$
{}^{T}\boldsymbol{J}_2={}^{2}_{5}\boldsymbol{R}^T\begin{bmatrix}0\\0\\1\end{bmatrix}=\begin{bmatrix}-\mathrm{s}h_2\,\mathrm{c}\theta_3\,\mathrm{c}h+\mathrm{c}h_2\,\mathrm{s}h\\ \mathrm{s}h_2\,\mathrm{s}\theta_3\\ \mathrm{s}h_2\,\mathrm{c}\theta_3\,\mathrm{s}h+\mathrm{c}h_2\,\mathrm{c}h\end{bmatrix},\ {}^{T}\boldsymbol{J}_4={}^{4}_{5}\boldsymbol{R}^T\begin{bmatrix}0\\0\\1\end{bmatrix}=\begin{bmatrix}\mathrm{s}h\\0\\ \mathrm{c}h\end{bmatrix}\tag{17}
$$

Ignoring the rotation of the end coordinate system around the z-axis, the Jacobian matrix can be expressed as

$$
{}^{T}\boldsymbol{J}=\begin{bmatrix}-\mathrm{s}h_2\,\mathrm{c}\theta_3\,\mathrm{c}h+\mathrm{c}h_2\,\mathrm{s}h & \mathrm{s}h\\ \mathrm{s}h_2\,\mathrm{s}\theta_3 & 0\end{bmatrix}\tag{18}
$$

Let the value of determinant $\sin h \sin h_2 \sin\theta_3=0$, and the solution is $\sin\theta_3=0$, which means that when DE and EG are collinear, the inverse kinematics singularity occurs.

Similarly, when BC is collinear with CG, it is also a singular state. Two collinear states are shown in Fig. 5 (b) and (c), respectively.

It is noteworthy that when $h > h_1 + h_2$, situation II will not occur; When $h < h_1 + h_2$, situation VI will not occur; When $h = h_1 + h_2$, situations II and VI occur at the same time, and the five links are located on the same plane.

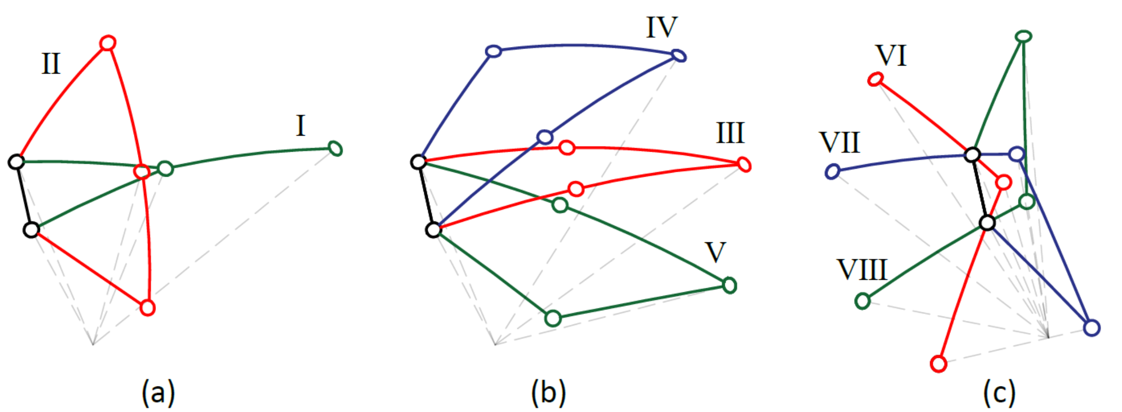

Fig. 5 Singularity of drive unit with non-zero-length ground link. (a) collinear of CG and GE, (b) straightening collinear, and (c) overlapping collinear

3 Conceptual Design of the Output Unit

According to the analysis results in Sec. 2, it can be seen that it is difficult to solve the forward kinematics of drive unit with non-zero-length ground link, and the singular configurations are complex. In addition, non-zero-length ground link drive unit cannot realize 360° rotation of yaw DOF like zero-length ground link drive unit. Hence, drive unit with zero-length ground link is selected as the drive for the proposed RCM mechanism.

To meet the operation requirements of surgical instruments, it is necessary to limit the rotation of the output shaft around its own axis, so that the instrument can be kept on the symmetrical plane of the mechanism. For the two solutions given in Fig. 6, an arc linkage with bevel gear constraint and a planar constraint branch are added on the basis of the spherical four-bar unit respectively.

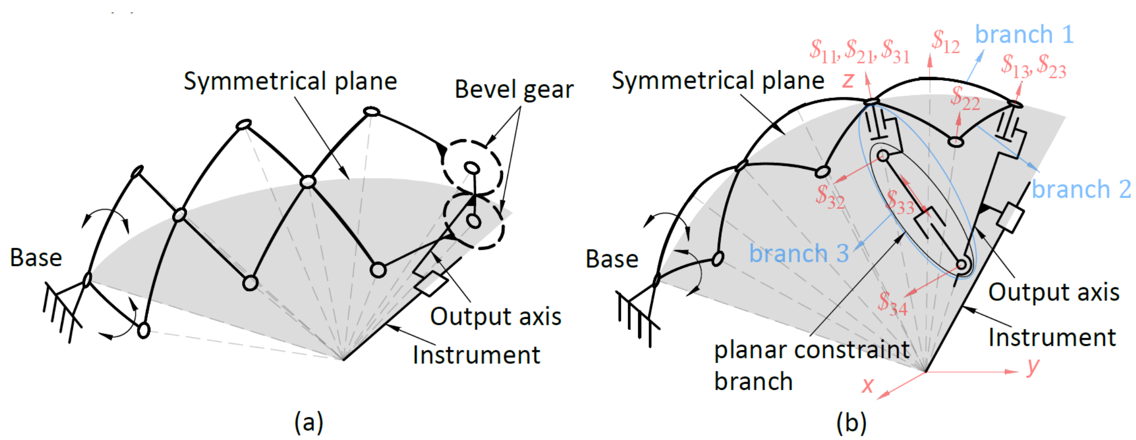

Fig. 6 Design of output unit. (a) Case 1: bevel gear constraint, and (b) Case 2: planar branch constraint

3.1 Analysis of Case 1

As shown in Fig. 6 (a), an arc linkage is added on the basis of the four-bar unit. To eliminate an extra degree of freedom, a gear constraint is added to form a symmetrical spherical five-bar unit, and the output axis is limited to the symmetrical plane of the spherical mechanism.

There are n =6 links and j =7 joints (including 6 revolute joints and 1 bevel gear joint) in the output unit of case 1. According to the Grülber-Kutzbach formula [19], the DOF of the mechanism is

$$F = d\left(n - j - 1\right) + \sum_{i=1}^{j} f_i + \upsilon - \xi = 3\left(6 - 7 - 1\right) + 6 + 2 = 2 \tag{19}$$

where $d = 6 - \lambda$ is the dimension of the space in which the mechanism is presented, $d = 6$ for spatial mechanism and $d = 3$ for planar and spherical mechanisms. Each joint has f_i degrees of freedom. The mechanism has λ common constraints, ν redundant constraints, and ζ local degrees of freedom. Through the test in the model, it is found that once any joint constraint is removed, the original motion cannot be realized, so there is no redundant constraint. All the components in the mechanism have no local motion so there is no local degree of freedom either.

3.1.1 Forward Kinematics

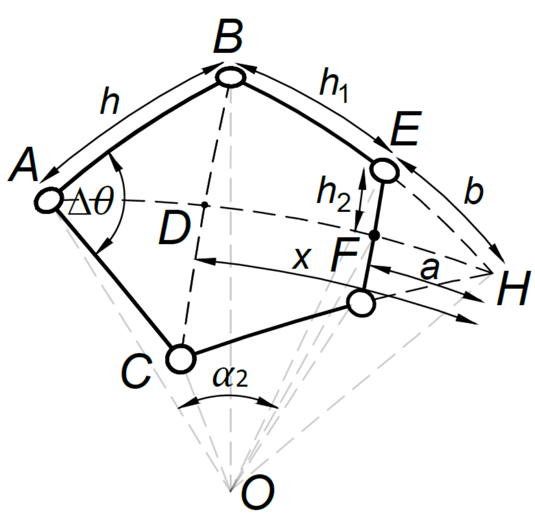

Fig. 7 Symmetrical five-bar spherical unit

The shape of the unit is only affected by $\Delta\theta$. As shown in Fig. 7, extend arc BE and arc CF intersect at point H, assuming that $\angle EOH = b$, $\angle FOH = a$, $\angle DOH = x$. It is known that, $\angle BOE = h_1$, $\angle EOF = h_2$, and the angles of all links are less than $\pi / 2$. The calculation method of $\angle AOD$ has been given in Sec. 2.1, and the calculation of $\angle DOF$ is carried out below.

Apply sine theorem on the spherical ΔEHF and ΔBHD

$$\begin{cases} \sin b = \sin h_2 / \sin \angle EHF \\ \sin\left(h_1 + b\right) = \sin \angle BOD / \sin \angle EHF \end{cases} \tag{20}$$

Thus,

$$b = \begin{cases} \tan^{-1}\left(\sin h_2 \sin h_1 / \left(\sin \angle BOD - \sin h_2 \cos h_1\right)\right) & \angle BEF \geqslant 90^\circ \\ \tan^{-1}\left(\sin h_2 \sin h_1 / \left(\sin \angle BOD - \sin h_2 \cos h_1\right)\right) + \pi & \angle BEF < 90^\circ \end{cases} \tag{21}$$

Apply cosine theorem on the spherical ΔEHF and ΔBHD

$$\begin{cases} a = \cos^{-1}\left(\cos b / \cos h_2\right) \\ x = \cos^{-1}\left(\cos\left(h_1 + b\right) / \cos \angle BOD\right) \end{cases} \tag{22}$$

The pitch angle of output axis can be obtained by substituting Eq. (1) and Eqs. (21-22) into the following formula.

$$\alpha_2 = \angle AOD + x - a \tag{23}$$

The calculation of yaw angle follows the same principle as Eq. (2).

3.1.2 Inverse Kinematics

Given α_2, $\angle AOE$ can be obtained by the spherical Pythagorean theorem. Apply cosine theorem on the spherical ΔEAF and ΔBAE to get

$$\angle EAF = \cos^{-1}\left(\frac{\cos h_2 - \cos\alpha_2 \cos\angle AOE}{\sin\alpha_2 \sin\angle AOE}\right)$$
$$\angle BAE = \cos^{-1}\left(\frac{\cos h_1 - \cos h \cos\angle AOE}{\sin h \sin\angle AOE}\right) \tag{24}$$

where $\angle AOE = \cos^{-1}\left(\cos h_2 \cos\alpha_2\right)$.

Thus, the driving angle

$$\Delta\theta = 2\left(\angle BAE + \angle EAF\right) \tag{25}$$

3.1.3 Singularity

Differentiating Eq. (23) yields

$$\frac{d\alpha_2}{dD} = -\frac{\cos h \cdot \sin D}{\cos D\sqrt{\cos^2 D - \cos^2 h}} - \frac{\cos D \cdot \sin H \cdot N + \sin D \cdot \cos H}{\cos D\sqrt{\cos^2 D - \cos^2 H}} + \frac{\sin b \cdot N}{\sqrt{\cos^2 h_2 - \cos^2 b}} \tag{26}$$

$$\frac{dD}{d\Delta\theta} = \frac{\sin^2 h \cdot \sin\Delta\theta}{2\sqrt{1 - \left(\cos^2 h + \sin^2 h \cdot \cos\Delta\theta\right)^2}} \tag{27}$$

$$J = \frac{d\alpha_2}{dD} \cdot \frac{dD}{d\Delta\theta} \tag{28}$$

where $N = \cos D \sin h_1 \sin h_2 / \left(\left(\sin D - \sin h_2 \cos h_1\right)^2 + \sin^2 h_1 \sin^2 h_2\right)$, D represents $\angle BOD$, and H represents $\angle BOH$. Then discuss the singularity in the range of $\Delta\theta \in \left(0, 180°\right)$ based on the above results.

(1) When $\Delta\theta = 0$, a triangle is formed at the end, resulting in an uncontrollable degree of freedom.

(2) When AB coincides with BE, $\sin D = \sin h \sin h_2 / \sin(h+h_1)$, and $b = \pi - (h+h_1)$. Substitute them into Eq. (28) and the numerator is 0, indicating that it is an inverse kinematics singularity.

(3) When BE coincides with EF, $\angle BOD = h_1 + h_2$, and $b = h_2$. At this time, the denominator of Eq. (28) is 0, indicating that it is a forward kinematics singularity. Note that this condition occurs only when $h > h_1 + h_2$.

3.2 Analysis of Case 2

The second solution, as shown in Fig. 6 (b), is by eliminating the rotation constraint of the output axis and another axis on the symmetry plane, and adding a planar constraint branch between two axes to limit the rotation of the output shaft.

According to the screw theory, the motion-screw systems of the three branches are:

$$
\begin{gathered}
\{\boldsymbol{S}_{l1}\} = \begin{Bmatrix} \boldsymbol{S}_{11} = (0,0,1,0,0,0)^{\mathrm{T}} \\ \boldsymbol{S}_{12} = (a_2,b_2,c_2,0,0,0)^{\mathrm{T}} \\ \boldsymbol{S}_{13} = (0,b_3,c_3,0,0,0)^{\mathrm{T}} \end{Bmatrix}, \{\boldsymbol{S}_{l2}\} = \begin{Bmatrix} \boldsymbol{S}_{21} = (0,0,1,0,0,0)^{\mathrm{T}} \\ \boldsymbol{S}_{22} = (-a_2,b_2,c_2,0,0,0)^{\mathrm{T}} \\ \boldsymbol{S}_{23} = (0,b_3,c_3,0,0,0)^{\mathrm{T}} \end{Bmatrix}, \\
\{\boldsymbol{S}_{l3}\} = \begin{Bmatrix} \boldsymbol{S}_{31} = (0,0,1,0,0,0)^{\mathrm{T}} \\ \boldsymbol{S}_{32} = (1,0,0,0,1,0)^{\mathrm{T}} \\ \boldsymbol{S}_{33} = (0,0,0,0,e_3,f_3)^{\mathrm{T}} \\ \boldsymbol{S}_{34} = (1,0,0,0,e_4,f_4)^{\mathrm{T}} \end{Bmatrix}
\end{gathered} \tag{29}
$$

where a_i, b_i, c_i, e_i, and f_i are parameters determined by the position of the screw.

According to the product of reciprocity is zero, each branch constraint-screw system is easily calculated,

$$\left\{\boldsymbol{S}_{li}^{r}\right\}=\left\{\begin{array}{l}\boldsymbol{S}_{i1}^{r}=\left(1,0,0,0,0,0\right)^{\mathrm{T}}\\ \boldsymbol{S}_{i2}^{r}=\left(0,1,0,0,0,0\right)^{\mathrm{T}}\\ \boldsymbol{S}_{i3}^{r}=\left(0,0,1,0,0,0\right)^{\mathrm{T}}\end{array}\right\},\left(i=1,2\right),\ \left\{\boldsymbol{S}_{l3}^{r}\right\}=\left\{\begin{array}{l}\boldsymbol{S}_{31}^{r}=\left(1,0,0,0,0,0\right)^{\mathrm{T}}\\ \boldsymbol{S}_{32}^{r}=\left(0,0,0,0,1,0\right)^{\mathrm{T}}\end{array}\right\} \tag{30}$$

The constraint-screw multiset of the output unit combines the three basis sets,

$$\left\langle \boldsymbol{S}^{r}\right\rangle=\left\{\boldsymbol{S}_{l1}^{r}\right\}+\left\{\boldsymbol{S}_{l2}^{r}\right\}+\left\{\boldsymbol{S}_{l3}^{r}\right\} \tag{31}$$

where card $\left\langle \boldsymbol{S}^{r}\right\rangle$ = 8. However, $\left\langle \boldsymbol{S}^{r}\right\rangle$ only contains four linearly independent screws, so a nonunique basis for the subspace $\boldsymbol{S}^{r}$ can be selected as

$$\left\{\boldsymbol{S}^{r}\right\}=\left\{\begin{array}{l}\boldsymbol{S}_{11}^{r}=\left(1,0,0,0,0,0\right)^{\mathrm{T}}\\ \boldsymbol{S}_{12}^{r}=\left(0,1,0,0,0,0\right)^{\mathrm{T}}\\ \boldsymbol{S}_{13}^{r}=\left(0,0,1,0,0,0\right)^{\mathrm{T}}\\ \boldsymbol{S}_{33}^{r}=\left(0,0,0,0,1,0\right)^{\mathrm{T}}\end{array}\right\} \tag{32}$$

Taking the reciprocal of $\boldsymbol{S}^{r}$ gives the motion-screw system $\boldsymbol{S}_{f}$ with the basis

$$\left\{\boldsymbol{S}_{f}\right\}=\left\{\begin{array}{l}\boldsymbol{S}_{f1}=\left(1,0,0,0,0,0\right)^{\mathrm{T}}\\ \boldsymbol{S}_{f2}=\left(0,0,1,0,0,0\right)^{\mathrm{T}}\end{array}\right\} \tag{33}$$

This shows that the output unit in case 2 has two rotational freedoms along the x-axis and z-axis respectively.

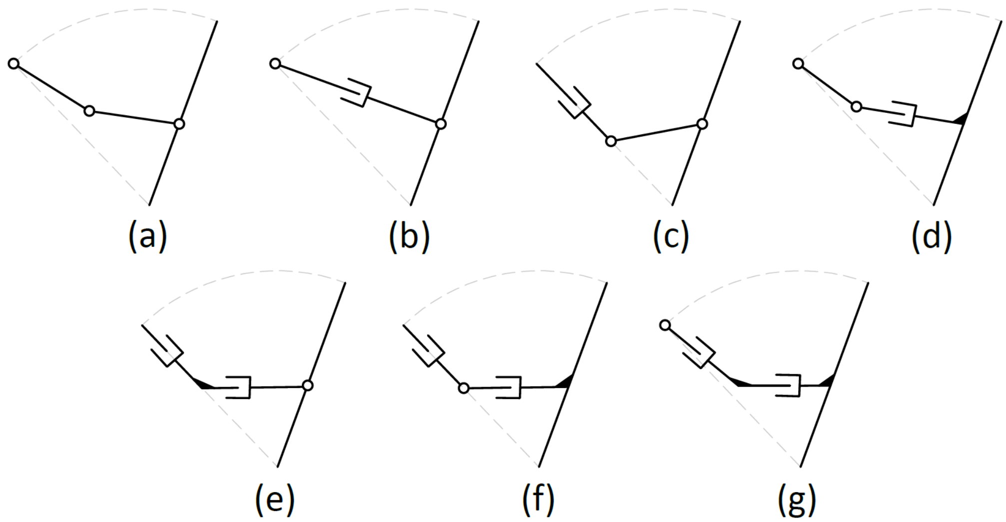

Fig. 8 Different configurations of planar constrain branch. (a) RRR branch, (b) RPR branch, (c) PRR branch, (d) RRP branch, (e) PPR branch, (f) PRP branch, and (g) RPP branch

It is observed that any planar branch containing three or more revolute or prismatic joints (and containing at least one revolute joint) in series with the revolute joint along the z-axis will produce a constraint equivalent to branch 3. According to the number and position of prismatic joints, the seven layouts in Fig. 8 meet the requirements. After verification in modeling software, it can be found that, the two prismatic joints in cases (e)-(g) are prone to interference. Comparing cases (b)-(d), case (b) has the advantage of compact structure. When the two links are collinear, case (a) will be singular. In conclusion, case (b) is the best choice.

4 Kinematic Model and Dimension Synthesis

According to the analysis result in Sec. 3, the forward kinematics of case 1 needs to be discussed separately. When it is used in series with spherical four-bar unit, the solution of inverse kinematics will also become very complex. In addition, the gear clearance may bring angle error to the end instrument.

4.1 Kinematic Model and Workspace of the spherical four-bar unit based RCM Mechanism

Based on the above analysis, the series structure composed of n spherical four-bar units combined with planar constraint branch in Fig. 6(b) is selected as the final solution. Thus, the kinematics model of the proposed RCM mechanism has an n-fold relationship with Eq. (2).

$$\begin{cases} \alpha_1 = 0.5\left(\theta_1 + \theta_2\right) \\ \alpha_2 = 2n\cos^{-1}\left(\cos h / \cos\left(0.5\cos^{-1}\left(\cos^2 h + \sin^2 h \cdot \cos\left(\theta_2 - \theta_1\right)\right)\right)\right) \end{cases} \tag{34}$$

In the analysis of the workspace, the critical state in which interference occurs needs to be considered. For yaw direction, 360° rotation can be achieved in any state. For pitch direction, due to the existence of solid material at each joint shaft, the linkages will collide near the singular position, which also makes the robot successfully avoid the singularity.

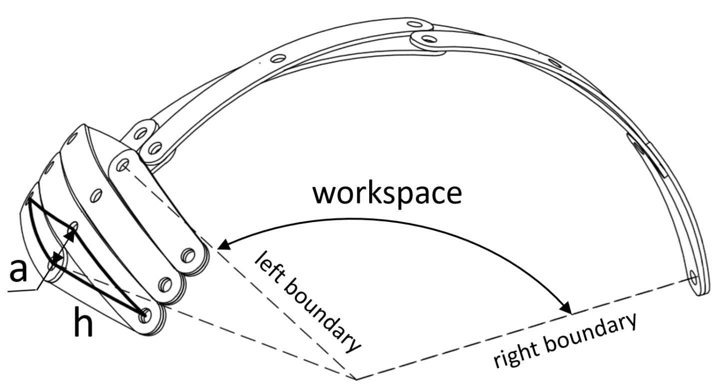

Fig. 9 Boundaries on both sides of the workspace

As shown in Fig. 9, assume that the width of the linkage is a. The arc length is approximately equal to the chord length when the angle value is small. Thus, the left boundary $\alpha_{2\min}$, the right boundary $\alpha_{2\max}$, and the total actual workspace α_{2all} can be approximately expressed as:

$$\alpha_{2\min}=na/r,\ \alpha_{2\max}=2n\cos^{-1}\left(\cos h/\cos\left(a/2r\right)\right),\ \alpha_{2all}=\alpha_{2\max}-\alpha_{2\min} \quad (35)$$

Therefore, the actual workspace is not only affected by the number of units n and the angle of linkages h, but also related to a and r. It can be seen from Eq. (35) that the smaller the rod width a, the larger the spherical radius r, the smaller the loss angle and the larger the total working space. In this mechanism, the minimum value of a is 30mm. Hence, the optimum dimensional synthesis of the mechanism can be summarized as: Given the workspace angle α_{2all}, determine n, h, and r such that the optimality of the global performance can be achieved.

4.2 Optimization and Dimension Synthesis

4.2.1 Object function

Due to the precise operation in the process of MIS, the robots need to have good operational flexibility for the needs of surgical safety. Simultaneously, in order to avoid interference among the multi-robot system, the occupied volume of the robot should also be considered. Therefore, in the process of dimension synthesis, two functions of operation performance index and compactness index should be considered.

The condition number κ of Jacobian matrix describes the uniformity of transformation in all directions [20-22]. The smaller the condition number, the closer the robot's movement ability in all directions.

The singular values of Jacobian matrix can be determined by solving the characteristic equation $det\left(\sigma^2 E - J \cdot J^T\right) = 0$. The results are $\sqrt{0.5}$ and $\left|\sqrt{2}Q\right|$ respectively, where $Q = \dfrac{n\sin^2 h \cdot \cos h \cdot \sin M \cdot \sin\Delta\theta}{\sqrt{1-\cos^2 2M} \cdot \sin\left(\alpha_2 / 2n\right) \cdot \cos^2 M}$, M is given in Eq. (5). It can be seen that the flexibility of the yaw direction is a constant, and the flexibility of the pitch direction changes with $\Delta\theta$.

$$\kappa = \frac{\sigma_2}{\sigma_1} = \begin{cases} \left|1/2Q\right| & \sqrt{0.5} \geqslant \left|\sqrt{2}Q\right| \\ \left|2Q\right| & \sqrt{0.5} < \left|\sqrt{2}Q\right| \end{cases} \tag{36}$$

Where σ_1 and σ_2 represent the minimum and maximum singular values respectively.

Considering that κ varies with the configuration of the robot, $\bar{\eta}$ and $\tilde{\eta}$ are used to describe the average value and fluctuation degree of global operational performance, respectively. The former index is similar to that proposed by Gosselin and Angeles [23].

$$\bar{\eta} = \int \kappa dW \Big/ \int dW = \frac{1}{\alpha_{2all}} \int_{\alpha_{2min}}^{\alpha_{2\max}} \kappa d\theta \tag{37}$$

$$\tilde{\eta} = \max\left(\kappa\right) / \min\left(\kappa\right) \tag{38}$$

Where $\min\left(\kappa\right)$ and $\max\left(\kappa\right)$ represent the minimum and maximum values of κ in working space W. Combining the mean value and the degree of fluctuation, the following global comprehensive performance index η can be constructed.

$$\eta = \sqrt{\bar{\eta}^2 + \left(\omega_\eta \tilde{\eta}\right)^2} \tag{39}$$

Where ω_η is the weight being placed upon the ratio of $\bar{\eta}$ to $\tilde{\eta}$.

In addition, the area occupied in the retracted state is taken as the compactness evaluation index.

$$s = b \times 2r \sin\left(\alpha_{2\min} / 2\right) \tag{40}$$

4.2.2 Constrains

According to the operation requirements of MIS, given the design objective: pitch workspace angle $\alpha_{2all} = 120°$. The constraints that the robot needs to meet are discussed below.

Firstly, in order to avoid interference between the instruments and patient's body in the preoperative adjustment process under specific posture, the minimum angle $\alpha_{2\min}$ in the retraction state needs to meet

$$\alpha_{2\min} \leqslant \theta_{\max} \tag{41}$$

Secondly, the spherical radius r should be sufficient to accommodate the end translational joint.

$$r \geqslant r_{\min} \tag{42}$$

When the robot retracts to the smallest angle, excessive width can easily lead to interference in the operation of multi-robot systems. So given the constraint

$$b = 2r \sin\left(\cos^{-1}\left(\cos h / \cos\left(a / 2r\right)\right)\right) \leqslant b_{\max} \tag{43}$$

Finally, an excessive number of motion units may lead to greater transmission error and increase assembly difficulty. Hence, a constraint associated with the number of motion units n should also be set such that

$$n_{\min} \leqslant n \leqslant n_{\max} \tag{44}$$

4.3 Implementation and Discussion

The optimum dimensional synthesis of the 2-DOF spherical mechanism can be regarded as the following constrained nonlinear programming problem:

$$\underset{x \in R^3}{\eta(x)} \rightarrow \min \tag{45}$$

subject to the constraints in Eqs. (41) throughout (44), where $x = \begin{pmatrix} n & r & h \end{pmatrix}^T$. Given $\omega_\eta = 0.6$, $\theta_{\max}$=30°, $r_{\min} = 460mm$, $b_{\max}$=300mm, $n_{\min} = 4$, $n_{\max} = 8$, and calculate the κ values in the workspace through bisection node method.

Figure 10 shows the variation of $\bar{\eta}$, $\tilde{\eta}$ and η with n and r in the range of $n = 5 \sim 8$ (When $n = 4$, the constraint conditions cannot be satisfied.) and $r = 350 \sim 750mm$. As shown in Fig. 10, both $\bar{\eta}$ and $\tilde{\eta}$ reduces firstly and increases afterward with the increase of r, but the position of the minimum value is different. Since the change of $\tilde{\eta}$ is more significant, the trend of η depends more on the change of $\tilde{\eta}$. In addition, the larger the number of units, the higher the flexibility that the mechanism can achieve, and the larger the optimal radius, indicating that improving the operating performance must be at the expense of increasing the volume.

When the constraints are met, draw η and s corresponding to different n into the broken line diagram in Fig. 11. and construct a comprehensive index of compactness and operability.

$$\xi = \sqrt{\eta^2 + \left(\omega_s s\right)^2} \tag{46}$$

Where ω_s is the weight being placed upon the ratio of η to s. In order to make η and s have equivalent values, let $\omega_s = 1/16000$ based on the ratio of the means of the two indexes. It can be seen that when $n=5$ and $r = 460mm$, the comprehensive performance of compactness and operability is the best.

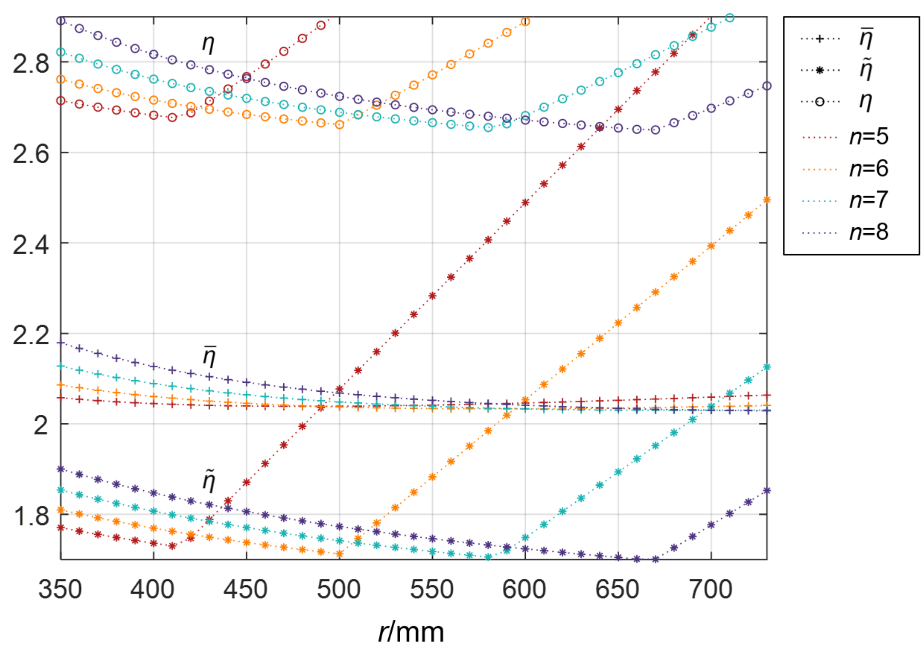

Fig. 10 Variations of $\bar{\eta}$, $\tilde{\eta}$ and η vs. spherical radius r and the number of units n, *where different color curves correspond to different* n *values.*

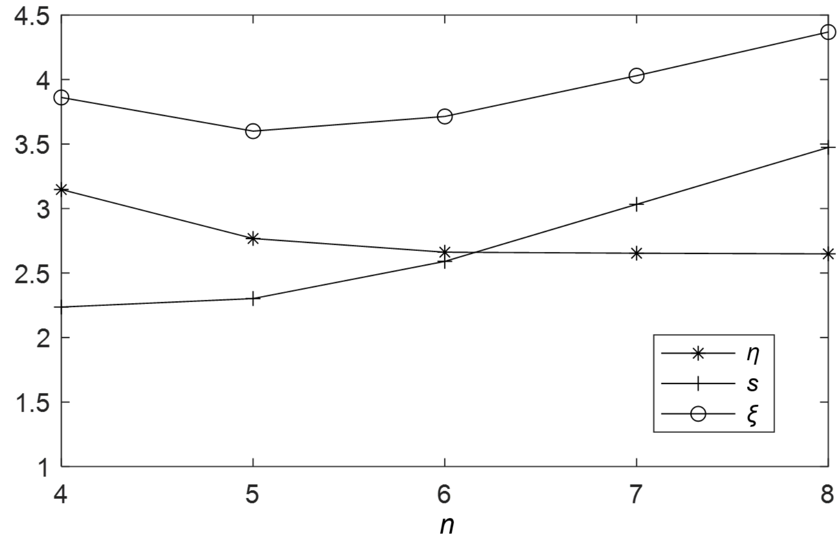

Fig. 11 Variations of η, s and ξ vs. the number of units n

Substituting $\alpha_{2all} = 120°$ into Eq. (35), and all the optimized structural parameters in Tab. 1 can be obtained.

Tab. 1 Optimized structural parameters

Parameters	n	r	h
Values	5	460mm	14°

5 Prototype and Error Evaluation

In order to verify the motion accuracy of the proposed RCM mechanism, a prototype as shown in Fig. 12 is design, fabricated and assembled according to the optimization results. When the robot is extended, the output linkage is far from the fixed base, in order to ensure the motion stability and structural stiffness, the first three groups of linkages near the fixed platform are made of stainless steel, and the other parts are made of aluminum alloy to reduce the impact of weight. On the other hand, the clearance of each revolute joint needs to be concerned. Increasing the contact thickness of the linkage relative to the diameter of the shaft hole will contribute to reducing the impact of joint clearance. Reference to the diameter of the hole 26 mm, a relatively larger 30mm was chosen as the thickness value here. Two servo motors are installed on the fixed platform in a compact manner, and the motion is transmitted through the bevel gear set with a reduction ratio of 2. And a translational joint is added at the end to realize one degree of freedom translation along the instrument axis. The parameters and variables of the prototype are shown in Tab. 2. The actual position error is measured by Leica AT960-MR absolute laser tracker of Hexagon Manufacturing Intelligence Company. The measurement setup is shown in Fig. 12(b).

Tab. 2 Parameters and variables of the prototype

Parameters	Values
Minimum pitch angle	$\alpha_{2\min} = 25.2°$
Maximum pitch angle	$\alpha_{2\max} = 145.4°$
Minimum radius of prototype	$R_{\min} = 460mm$
Maximum radius of prototype	$R_{\max} = 532mm$
Maximum width of prototype	$B_{\max} = 284mm$

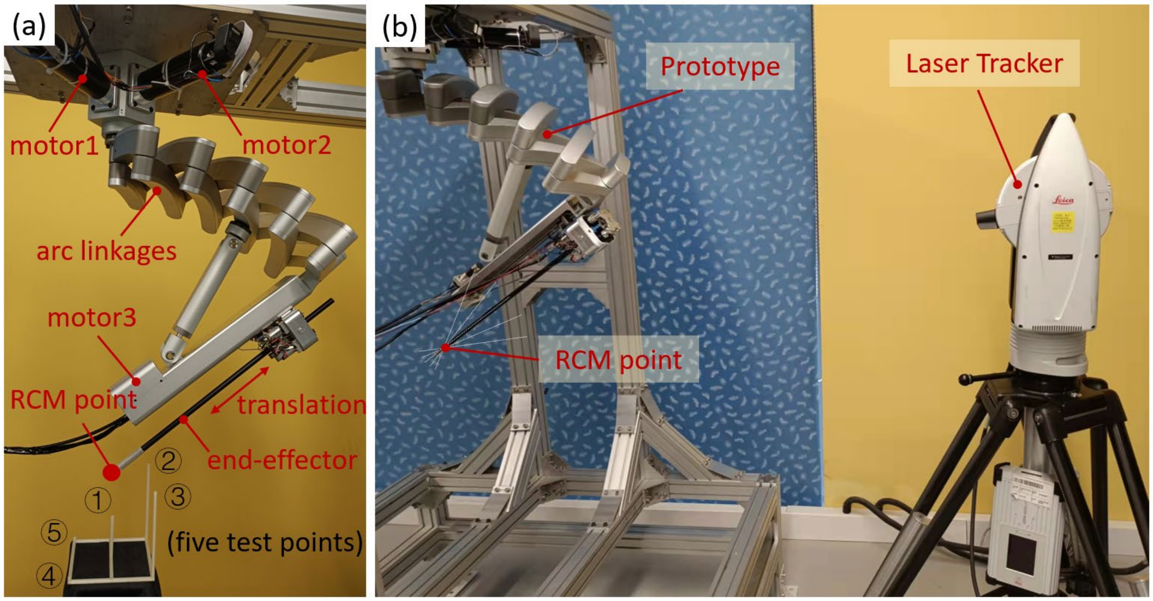

Fig. 12 Prototype of the proposed RCM mechanism. (a) composition of prototype, and (b) experimental measurement setup

The repeated positioning accuracy of the robot was first measured. As shown in Fig. 12(a), the parameters of the three motors are adjusted to control the 2R1T motion of the robot so that the end of the instrument reaches the five test points in turn. Setting the velocity of the end point as 5cm/s, the control program is cycled 10 times and the co-ordinate values of the end point of the instrument are recorded by the laser tracker. The experimental data obtained are given in Fig. 13(a)-(e), where the solid red dots are the average of each set of data. The distance between the average point and the furthest data point is defined as the repeated positioning error (length of the red line segment in the figure), and the calculations are summarized in Fig. 13(f). The repeated positioning errors at each point are 0.12mm, 0.14mm, 0.15mm, 0.16mm and 0.13mm respectively. The repeated positioning accuracy of this robot is relatively high, so it can be inferred that the return error caused by joint clearance is very small.

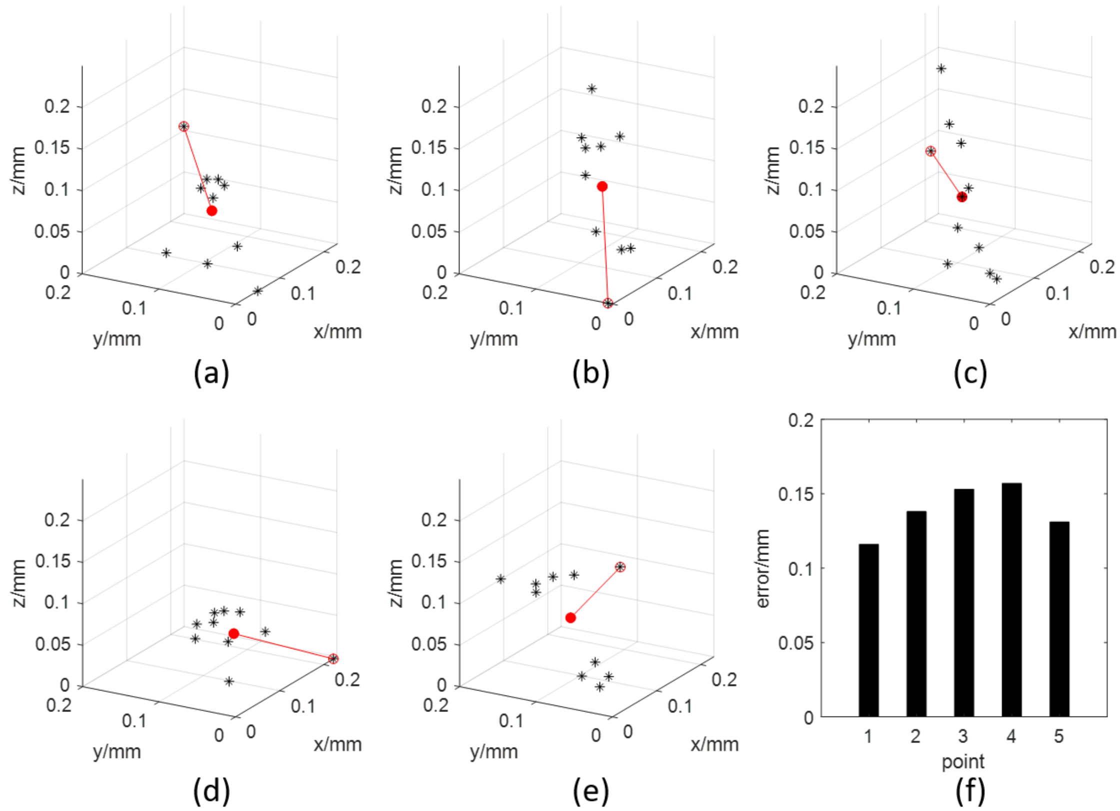

Fig. 13 The results of repeated positioning accuracy

Next, the misalignment of the end instrument is measured to verify the RCM characteristics of the prototype. The end point of the instrument is made to coincide with the RCM point in the axial direction, and then the 2-DOF rotations are adjusted to drive the robot to each of the 5 x 6 = 30 states in Fig. 14. The pitch angle is between 25° and 145° and the yaw angle is between -60° and 60°. Figure 15 shows the distance error between the end point of the instrument and the standard RCM point in all acquisition attitudes. The maximum and mean values of these errors are 1.06 mm and 0.56 mm respectively.

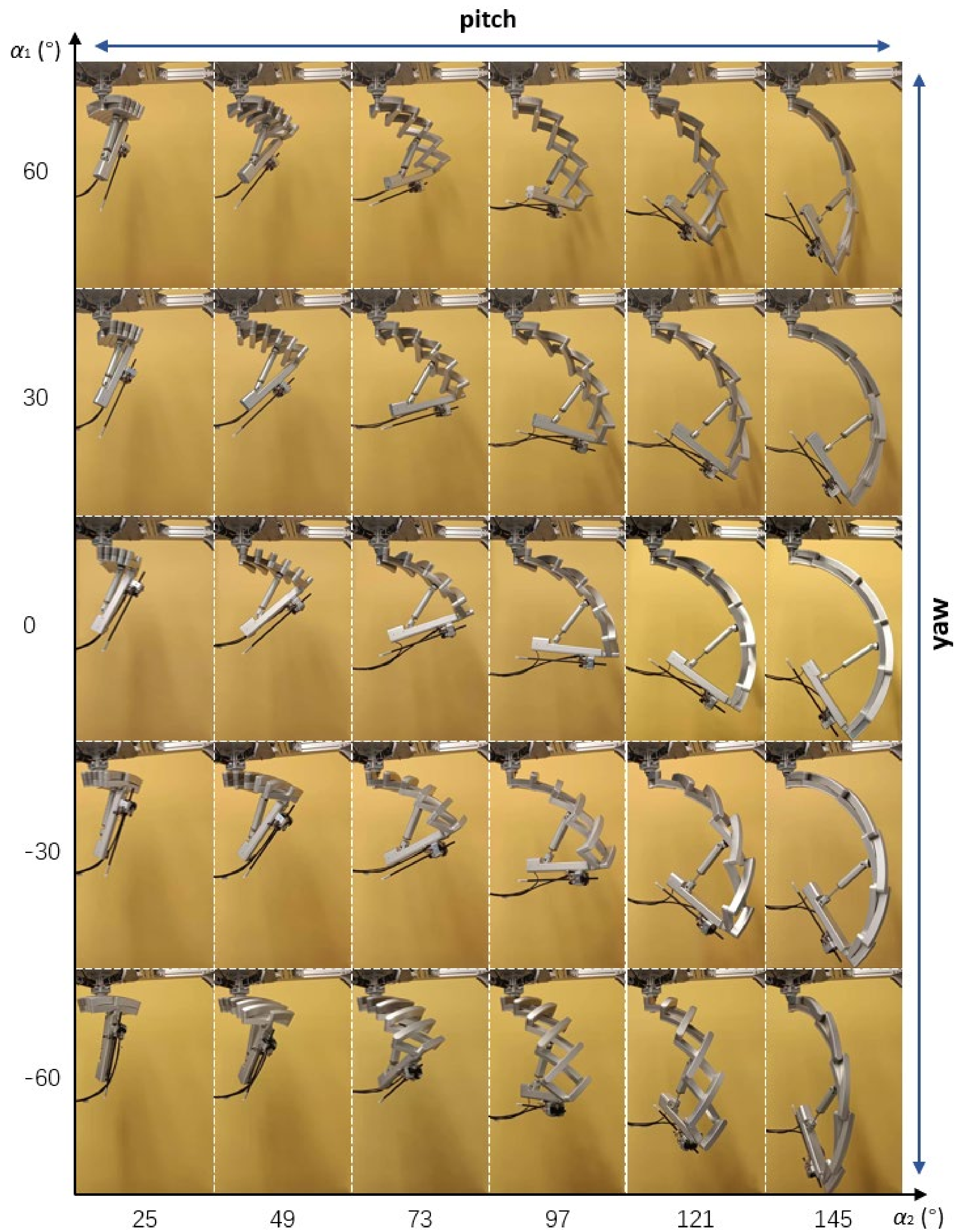

Fig. 14 Workspace division of the developed RCM prototype

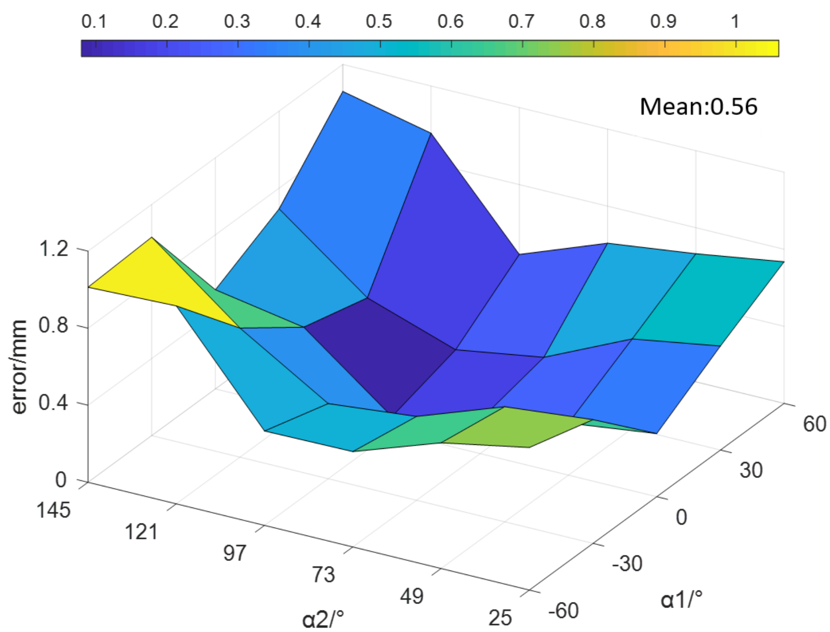

Fig. 15 The position error of the RCM point

It is noteworthy that the position error of general MIS robot should be within 2 mm [24]. Therefore, it can be considered that the developed RCM prototype can provide a stable remote center for surgical tasks. When α_1 deviates from 0°, the position error of the developed prototype will increase accordingly. When α_2 deviates from 90°, the position error increases at a more significant rate. This indicates that the yaw accuracy is slightly higher than the pitch accuracy. Considering the randomness of gear clearance, manufacturing error and assembly error, the experimental results are completely acceptable. In the future work, the accuracy of the prototype can be further improved by using high-precision manufacturing and assembly technology, initial configuration calibration technology and structural optimization. Therefore, it is believed that the proposed RCM robot with unique structure has potential application in MIS robot.

6 Conclusions

In conclusion, the mechanism proposed in this paper utilizes the spherical unit to keep all links on the spherical surface with fixed radius, which greatly improves the compactness of the mechanism. It is a major improvement of the existing surgical robot. The mechanism has high volume expansion rate, easy to realize modular design, and can meet the needs of workspace in different situations by increasing or reducing the number of units. For the pitch direction, the existence of solid material at the joints makes the mechanism free from singularity. For yaw direction, 360° rotation can be achieved in any state. For different workspace and constraints, the optimal structural parameters of the mechanism can be determined by dimensional synthesis with the goal of optimal global operation performance. Moreover, an experimental prototype was developed to verify the feasibility of the proposed RCM mechanism. The results show that the repetitive positioning accuracy of the mechanism is within 0.2mm, and the RCM point accuracy is within 1.1mm. Therefore, the proposed 2-DOF RCM mechanism can be used as a precision manipulator for MIS completely.

ACKNOWLEDGMENT

This work is supported by the National Natural Science Foundation of China under Grants 52122501, 51875394, and 52075277, and Science and Technology Program of Tianjin under grant 20JCZDJC00790.

APPENDIX

Before manufacturing the prototype, finite element simulation is performed to adjust the material and structural details. A 20 N load force and a 5 N tissue operating force are applied to the end of the curved linkage and the end of the instrument, respectively, and a ground gravitational force is applied. It can be seen that the optimized model has more uniform stress and strain and less deformation.

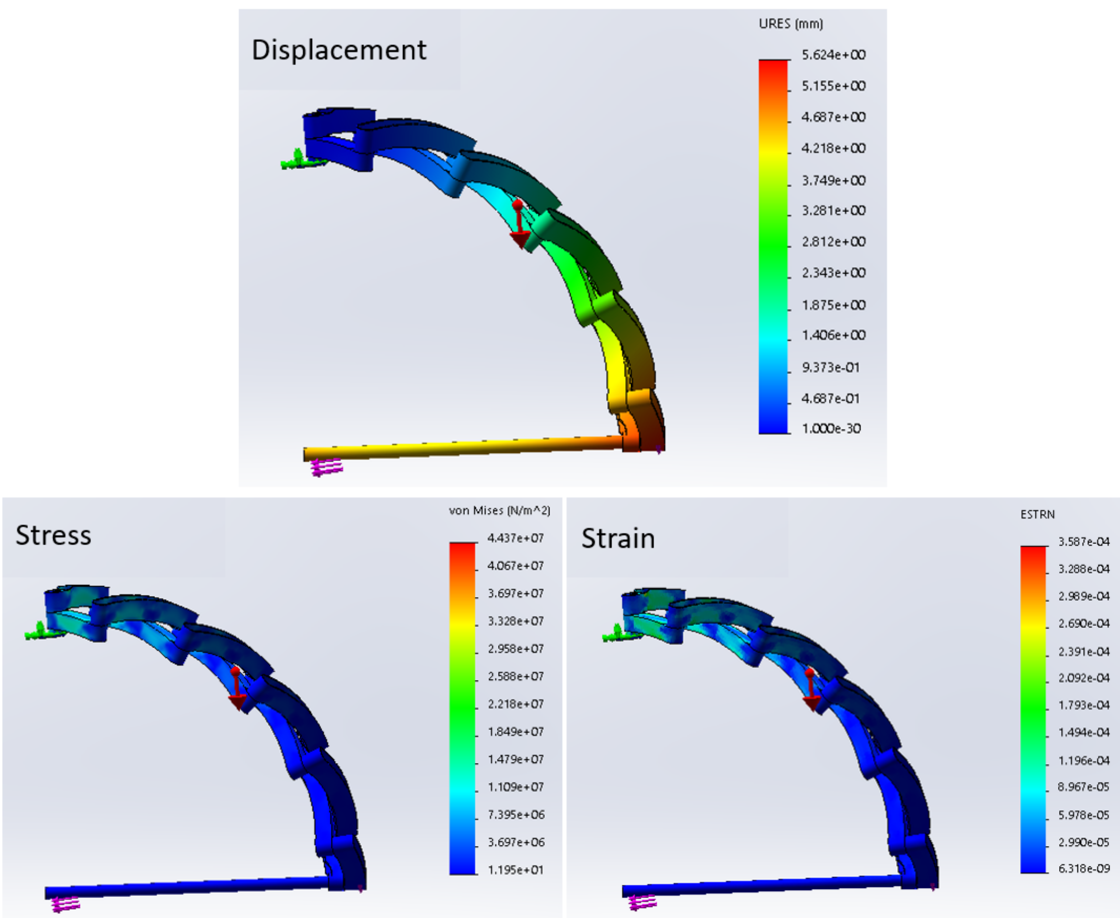

Fig. A1 Finite element simulation results before optimization

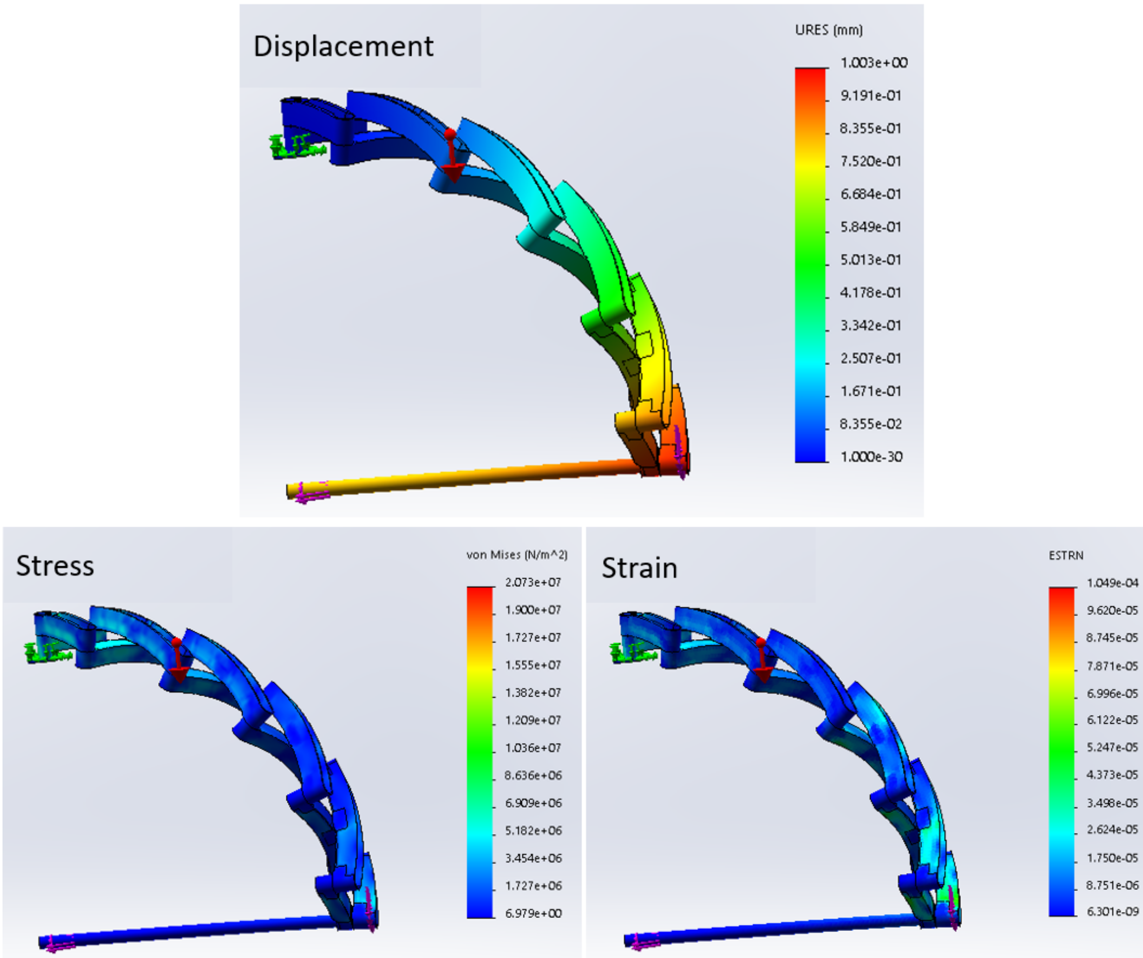

Fig. A2 Finite element simulation results after optimization

REFERENCES

[1] Kuo, C. H., Dai, J. S., and Dasgupta, P., 2012, “Kinematic design considerations for minimally invasive surgical robots: an overview,” International Journal of Medical Robotics and Computer Assisted Surgery, 8(2), pp. 127-145. DOI: 10.1002/rcs.453

[2] Dai, J. S., 2010, “Surgical Robotics and Its Development and Progress,” Robotica, 28(S2), pp. 161-161. DOI: 10.1017/S0263574709990877

[3] Locke, R. C. O., and Patel, R. V., 2007, “Optimal Remote Center-of-Motion Location for Robotics-Assisted Minimally Invasive Surgery,” IEEE International Conference on Robotics and Automation, Rome, April 10-14, pp. 1900-1905.

[4] Taylor, R. H., and Stoianovici, D., 2003, "Medical Robotics in Computer–Integrated Surgery," IEEE Translation on Robotics and Automation, 19(5), pp. 765-781. DOI: 10.1109/TRA.2003.817058

[5] Li, J. M., Zhang, G. K., Xing, Y., Liu, H. B., and Wang, S. X., 2016, "A Class of 2-Degree-of-Freedom Planar Remote Center-of-Motion Mechanisms Based on Virtual Parallelograms," Journal of Mechanisms and Robotics-Transactions of the ASME, 6(3), pp. 031014.1-7. DOI: 10.1115/1.4027239

[6] Huang, L., Yin, L. R., Liu, B., and Yang, Y., 2021, "Design and Error Evaluation of Planar 2DOF Remote Center of Motion Mechanisms with Cable Transmissions," Journal of Mechanical Design-Transactions of the ASME, 143(1), pp. 013301.1-12. DOI: 10.1115/1.4047519

[7] Kuo, C. H., and Dai, J. S., 2012, "Kinematics of a Fully-Decoupled Remote Center-of-Motion Parallel Manipulator for Minimally Invasive Surgery," Journal of Medical Devices-Transactions of the ASME, 6(2), pp. 021008.1-12. DOI: 10.1115/1.4006541

[8] Chen, G. L., Wang, J., Wang, H., Chen, C., Parenti-Castelli, V., and Angeles, J., 2020, "Design and validation of a spatial two-limb 3R1T parallel manipulator with remote center-of-motion," Mechanism and Machine Theory, 149, pp. 1-18. DOI: 10.1016/j.mechmachtheory.2020.103807

[9] Liu, S., Chen, B., Caro, S., Briot, S., Harewood, L., and Chen, C., 2016, "A Cable Linkage with Remote Center of Motion," Mechanism and Machine Theory, 105, pp. 583-605. DOI: 10.1016/j.mechmachtheory.2016.07.023

[10] Liu, S., Harewood, L., Chen, B., and Chen, C., 2016, "A Skeletal Prototype of Surgical Arm Based on Dual-Triangular Mechanism," Journal of Mechanisms and Robotics-Transactions of the ASME, 8(4), pp. 041015.1-7. DOI: 10.1115/1.4032976

[11] Zhang, X. L., and Nelson, C. A., 2008, "Kinematic Analysis and Optimization of a Novel Robot for Surgical Tool Manipulation," Journal of Medical Devices-Transactions of the ASME, 2(2), pp. 021003.1-8. DOI: 10.1115/1.2918740

[12] Nabil, Z., and Guillaume, M., 2007, "Mechatronic Design of a New Robot for Force Control in Minimally Invasive Surgery," IEEE-ASME Transactions on Mechatronics, 12(2), pp. 143-153. DOI: 10.1109/TMECH.2007.892831

[13] Roovers, K., and De Temmerman, N., 2017, "Deployable Scissor Grids Consisting of Translational Units," International Journal of Solids and Structures, 121, pp.45-61. DOI: 10.1016/j.ijsolstr.2017.05.015

[14] Mira, L. A., Coelho, R. F., Thrall, A. P., and De Temmerman N., 2015, “Parametric Evaluation of Deployable Scissor Arches,” Engineering Structures, 99, pp. 479-491. DOI: 10.1016/j.engstruct.2015.05.013

[15] Mira, L. A., Thrall, A. P., and De Temmerman N., 2014, “Deployable Scissor Arch for Transitional Shelters,” Automation in Construction, 43, pp. 123-131. DOI: 10.1016/j.autcon.2014.03.014

[16] Kocabas, H., 2009, “Gripper Design with Spherical Parallelogram Mechanism,” Journal of Mechanical Design-Transactions of the ASME, 131(7), pp. 075001.1-9. DOI: 10.1115/1.3125891

[17] Castro, M. N., Rasmussen, J., Andersen, M. S., and Bai, S. P., 2019, “A Compact 3-DOF Shoulder Mechanism Constructed with Scissors Linkages for Exoskeleton Applications,” Mechanism and Machine Theory, 132, pp. 264-278. DOI: 10.1016/j.mechmachtheory.2018.11.007

[18] Afshar, M., Carriere, J., Meyer, T., Sloboda, R., Husain, S., Usmani, N., and Tavakoli, M., 2020, “Optimal Design of a Novel Spherical Scissor Linkage Remote Center of Motion Mechanism for Medical Robotics”, 2020 IEEE/RSJ International Conference on Intelligent Robots and Systems, Las Vegas, NV, USA, pp. 6459-6465. DOI: 10.1109/IROS45743.2020.9341365

[19] Dai, J.S., Huang, Z. and Lipkin, H., 2006, “Mobility of Overconstrained Parallel Mechanisms,” Journal of Mechanical Design-Transactions of the ASME, 128(1), pp. 220-229. DOI: 10.1115/1.1901708

[20] Gosselin, C. M., 1990, “Dexterity indices for planar and spatial robotic manipulators,” Proceedings., IEEE International Conference on Robotics and Automation, Cincinnati, OH, USA, pp. 650-655. DOI: 10.1109/ROBOT.1990.126057

[21] Huang, T., Whitehouse, D. J., and Wang, J. S., 1998, ‘‘The Local Dexterity, Optimum Architecture and Design Criteria of Parallel Machine Tools,’’ CIRP Annals, 47(1), pp. 347-351.

[22] Huang, T., Wang, J. S., Gosselin, C. M., and Whitehouse, D. J., 2000, ‘‘Kinematic Synthesis of Hexapods with Prescribed Orientation Capability and Well-Conditioned Dexterity,’’ Journal of Manufacturing Processes, 2(1), pp. 36-47.

[23] Gosselin, C. M., and Angeles, J., 1991, ‘‘A Globe Performance Index for the Kinematic Optimization of Robotic Manipulators,’’ Journal of Mechanical Design-Transactions of the ASME, 113(3), pp. 220-226.

[24] Ferguson, J. M., Cai, L. Y., Reed, A., Siebold, M., De, S., Herrell, S. D., and Webster, R. J., 2018, “Toward Image-Guided Partial Nephrectomy with the Da Vinci Robot: Exploring Surface Acquisition Methods for Intraoperative Re-Registration,” Proceedings of SPIE, 10576, pp. 1057609. DOI: 10.1117/12.2296464

Figure Captions List

Fig. 1	Comparison of two kinds of spherical RCM mechanisms. (a) traditional spherical mechanism, and (b) the proposed spherical scissor-like linkage mechanism
Fig. 2	Design of drive unit. (a) Case 1: drive unit with zero-length ground link, and (b) Case 2: drive unit with non-zero-length ground link
Fig. 3	Singularity of drive unit with zero-length ground link
Fig. 4	Drive unit with non-zero-length ground link
Fig. 5	Singularity of drive unit with non-zero-length ground link. (a) collinear of $\boldsymbol{CG}$ and $\boldsymbol{GE}$, (b) straightening collinear, and (c) overlapping collinear
Fig. 6	Design of output unit. (a) Case 1: bevel gear constraint, and (b) Case 2: planar branch constraint
Fig. 7	Symmetrical five-bar spherical unit
Fig. 8	Different configurations of planar constrain branch. (a) RRR branch, (b) RPR branch, (c) PRR branch, (d) RRP branch, (e) PPR branch, (f) PRP branch, and (g) RPP branch
Fig. 9	Boundaries on both sides of the workspace
Fig. 10	Variations of $\bar{\eta}$, $\tilde{\eta}$ and η vs. spherical radius r and the number of units n, *where different color curves correspond to different* n *values*.
Fig. 11	Variations of η, s and ξ vs. the number of units n
Fig. 12	Prototype of the proposed RCM mechanism. (a) composition of prototype, and (b) experimental measurement setup
Fig. 13	The results of repeated positioning accuracy
Fig. 14	Workspace division of the developed RCM prototype
Fig. 15	The position error of the RCM point

Table Caption List